



Science Arts & Métiers (SAM)

is an open access repository that collects the work of Arts et Métiers Institute of Technology researchers and makes it freely available over the web where possible.

This is an author-deposited version published in: <https://sam.ensam.eu>
Handle ID: <http://hdl.handle.net/10985/18000>

To cite this version :

Fawzi FADLA, Frédéric ALIZARD, Laurent KEIRSBULCK, Jean-Philippe LAVAL, Jean-Marc FOUCAUT, Camila CHOVET, Marc LIPPERT, Jean-Christophe ROBINET - Investigation of the dynamics in separated turbulent flow - European Journal of Mechanics - B/Fluids - Vol. 76, p.190-204 - 2019

Any correspondence concerning this service should be sent to the repository

Administrator : scienceouverte@ensam.eu



Investigation of the dynamics in separated turbulent flow

Fawzi Fadla^b, Frederic Alizard^a, Laurent Keirsbulck^{b,*}, Jean-Christophe Robinet^e,
Jean-Philippe Laval^{c,d}, Jean-Marc Foucaut^d, Camila Chovet^b, Marc Lippert^b

^a LMFA, CNRS École Centrale de Lyon, Université, Lyon 1, INSA, Lyon, France

^b LAMIH CNRS UMR 8201, F-59313, Valenciennes, France

^c CNRS, ONERA Arts et Metiers ParisTech, Lille, France

^d Centrale Lille, FRE 3723-LMFL-Laboratoire de Mécanique des Fluides de Lille-Kampé de Férie, France

^e DynFluid EA92, F-75013, Paris, France

A B S T R A C T

Dynamical behavior of the turbulent channel flow separation induced by a wall-mounted two-dimensional bump is studied, with an emphasis on unsteadiness characteristics of vortical motions evolving in the separated flow. The present investigations are based on an experimental approach and Direct Numerical Simulation (DNS). The main interests are devoted to give further insight on mean flow properties, characteristic scales and physical mechanisms of low-frequencies unsteadiness. The study also aims to clarify the Reynolds number effects. Results are presented for turbulent flows at moderate Reynolds-number Re_τ ranging from 125 to 730 where Re_τ is based on friction velocity and channel half-height. A large database of time-resolved two-dimensional PIV measurements is used to obtain the velocity distributions in a region covering the entire shear layer and the flow surrounding the bump. An examination of both high resolved velocity and wall-shear stress measurements showed that for moderate Reynolds numbers, a separated region exists until a critical value. Under this conditions, a thin region of reverse flow is formed above the bump and a large-scale vortical activity is clearly observed and analyzed. Three distinct self-sustained oscillations are identified in the separated zone. The investigation showed that the flow exhibits the shear-layer instability and vortex-shedding type instability of the bubble. A low-frequency self-sustained oscillation associated with a flapping phenomenon is also identified. The experimental results are further emphasized using post-processed data from Direct Numerical Simulations, such as flow statistics and Dynamic Mode Decomposition. Physical mechanisms associated with observed self-sustained oscillations are then suggested and results are discussed in the light of instabilities observed in a laminar regime for the same flow configuration.

1. Introduction

Turbulent boundary layer separation, mean flow patterns and unsteady behavior, play an important role in a wide range of industrial applications. In this context, several research efforts have been focused on improving current technologies of ground vehicles and aircraft with a specific attention devoted to social and environmental issues. Flow separation generally causes an increase of drag force associated with a strong lift reduction, and consequently leads to significant losses of aerodynamic performances (e.g. Joseph et al. [1] and Yang and Spedding [2]). Moreover, the unsteadiness exhibited in turbulent boundary layer separation (referenced as TSB "Turbulent Separated Bubble" hereafter) create large pressure fluctuations that act as strong aerodynamic loads.

The prediction of the associated critical parameters is essential in the vibro-acoustic design of many engineering applications. In that respect, several attempts have been made to investigate active flow control strategies (see Dandois et al. [3] for instance). Despite all these efforts, major issues, related to accurate predictions of the mean separation point or the understanding of the origin of turbulent separated flow unsteadiness, are still under debate. Consequently, the boundary layer separation prediction as well as its control has been considered as major challenge for years [4]. Separation process is commonly encountered in wall-bounded flows subjected to an adverse pressure gradient or to an abrupt geometry variation.

Many research activities have been focused on relatively simple academic configurations such as a rounded ramp [5], a bump [6], a wall-mounted bump [7–10], a backward facing step [11] or a thick flat plate [12,13].

All these investigations pointed out complex flow physics associated with TSB (i.e. a wide range of temporal and spatial scales). In particular, recently Mollicone et al. [9] have conducted intensive channel flow simulations with the presence of a bump on the lower wall which produces the flow separation. The authors give some insight onto the role of the different terms in the kinetic energy budget of the mean flow. The anisotropy of the different scales are also highlighted through the deviatoric components of the Reynolds stresses aiming to improve turbulence modeling for separated flows. Mollicone et al. [10] expanded these analyses by trying to identify the link with coherent structures through the generalized Kolmogorov equation (GKE). However, a further understanding onto the role of coherent vortical motion and flow unsteadiness are not discussed by Mollicone et al. [9] and Mollicone et al. [10].

Different unsteadiness types are generally encountered in TSB, as shown experimentally by Cherry et al. [14] and Kiya and Sasaki [12], for a flow over a blunt plate held normal to a uniform stream and for a backward facing step by Eaton and Johnston [15]. Experimental evidences of Cherry et al. [14] and Kiya and Sasaki [12] are further confirmed numerically by Tafti and Vanka [16]. Instabilities associated with the roll-up of the shear layer are identified by the authors cited above. They exhibit similarities with turbulent mixing layer experiments of Brown and Roshko [17], who first linked the emergence of large scale spanwise-coherent rollers with instabilities properties of the mean turbulent flow. The Strouhal number for the vortex shedding is measured by Cherry et al. [14] and Kiya and Sasaki [12] $S_f \approx 0.6 - 0.7 U_\infty / L_R$, where U_∞ is the free-stream velocity and L_R is the mean recirculation length. While previous authors gave a scaling based on L_R , Sigurdson [18] suggested a characteristic length scale associated with the bubble height for the same flow case. As recently underlined by Marquillie et al. [19], near wall coherent turbulent streaks (see Cossu et al. [20] for instance) may also interact with TSB and generate vortex shedding.

It is also shown by Cherry et al. [14] and Eaton and Johnston [15] that the separation line oscillates at a low frequency of the order $S_f \approx 0.12 - 0.2$, the so-called flapping motion. These authors argued that the cause of the low frequency unsteadiness is an instantaneous imbalance between the entrainment rate from the bubble and the reinjection of fluid near the reattachment line. Pionniau et al. [21] proposed a similar mechanism for low-frequency unsteadiness observed in shock-induced separation for supersonic flows. In this context, the latter authors derived a simple model based on time averaged values of the separated flow that seems to be consistent with experiments and numerical simulations for both subsonic and supersonic flows. Kiya and Sasaki [12] proposed another scenario to explain the flapping phenomenon that is based on a pressure feedback mechanism linked to the oscillating reattachment line. Finally, while Eaton and Johnston [15] argued that the mechanism is mainly two-dimensional, Tafti and Vanka [16] have shed some light on the importance of three-dimensional effects. Hence, from this discussion, it seems that there is not a consensus on the driving mechanism associated with the flapping motion and the characteristic scales of the vortex shedding frequency.

Similar flow unsteadiness such as flapping phenomenon or Kelvin–Helmholtz instabilities are also observed in a laminar separated flow (see Dovgal et al. [22]). In particular, based on the preliminary work of Brown and Roshko [17] who gives some insight about similarities between laminar and turbulent large scale structures, Marquillie and Ehrenstein [23] and Ehrenstein and Gallaire [24] have investigated the onset of low-frequencies unsteadiness in the case of a laminar separated flows at the rear of a bump. For that purpose, previous authors carried out Direct Numerical Simulations and stability analyses. One may

recall that unsteadiness in open-flows can be classified into two main categories (see Huerre and Monkewitz [25] and Chomaz [26] for a review).

The flow can behave as an oscillator (i.e. due to a global unstable mode) where self-sustained oscillations are observed. Or the flow may exhibit a noise-amplifier dynamics due to convective instabilities. In that case, the flow filters and amplifies upstream perturbations. In this context, Ehrenstein and Gallaire [24] attributed the emergence of the flapping motion to an oscillator dynamics caused by the interference of linear Kelvin–Helmholtz modes spatially extended in the entire bubble. Passaggia et al. [27] provided further arguments on this mechanism by carrying out several experiments. Nevertheless, for the case of a flat plate separated flow, Marxen and Rist [28] pointed out the strong influence of nonlinearities on low frequencies unsteadiness. In addition, the latter authors suggested that flapping phenomenon may be triggered by a forcing upstream the separated zone similar as a noise amplifier flow dynamic. The importance of the noise amplifier mechanism to generate large scale motions in laminar separated flows is also highlighted by Alizard et al. [29], Marquet et al. [30] and Blackburn et al. [31]. Gallaire et al. [32], Passaggia et al. [27] and Barkley et al. [33] have shown that initially two-dimensional recirculation bubble can exhibit three-dimensional resonator dynamics that triggers spanwise modulation and vortex shedding (see Robinet [34] for a recent review). However, no effort has been made to provide characteristic length scales and a link with the turbulent regime.

The dynamics of a turbulent separated flow, whether behind a hump or more generally behind a surface defect (backward-facing step, forward-facing step, ...) is representative of many industrial configurations. Furthermore, a large number of separated flows are the seat of a low-frequency motions. From the discussion above, low-frequency dynamics is a common characteristic shared by many separated flow configurations for various flow regimes (subsonic, transonic and supersonic). The objective of this paper is to study the dynamics of a turbulent separated flow with a particular focus on its dependence upon Reynolds number. The latter parameter has a major impact on flow unsteadiness because shaping the mean flow, *i.e.* its characteristic length scales. We will consider hereafter the same case as the one studied by Marquillie and Ehrenstein [23] and Passaggia et al. [27] but for a turbulent flow, which has been not considered yet. We aim to provide spatial and temporal characteristic scales of unsteadiness associated with the turbulent regime and give some insight about the underlying large scale coherent structures.

The present study will thus address some fundamental questions such as the following: how does the Reynolds-number affect the mean separation length and turbulence statistics? Does turbulent separated flow at the rear of a bump exhibit similar flow unsteadiness as those observed in other TSB cases? What are the spatial and temporal characteristic scales associated with flow unsteadiness and does the flow exhibit similar coherent structures as those found in a laminar regime?

To this purpose, high-resolution particle image velocimetry and electrochemical experimental measurements have been conducted in a separated flow at the friction Reynolds-number $Re_\tau = 125 - 730$. An electrochemical experimental measurement determines the limiting diffusion current at the surface of a platinum microelectrode in order to calculate the wall bounded turbulent flow dynamics. Three-dimensional direct numerical simulations have also been performed in the same Reynolds number range ($Re_\tau = 187, 395$ and 617). One may precise that no detailed quantitative experimental comparison to these numerical simulations in such configuration has been made up-to-now.

The paper is thus organized as follows. The apparatus, the experimental techniques and the flow parameters are given in

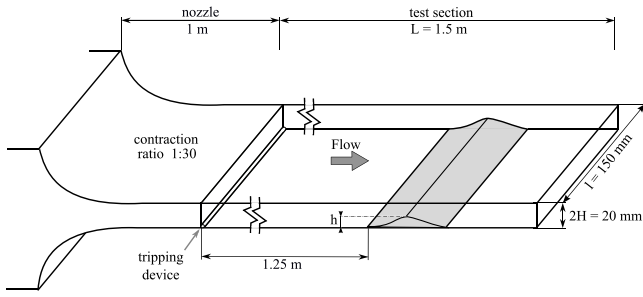


Fig. 1. 3D view of the channel setup.

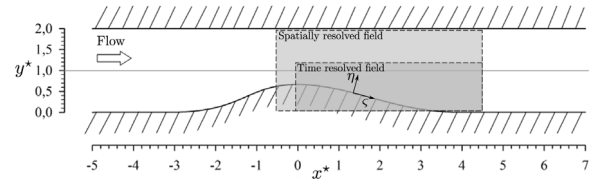


Fig. 2. Test section containing the two-dimensional bump geometry and the Piv fields of interest. The symbol \star denotes the half height normalization. η represents the direction of the local outward normal of the surface and ζ the tangential direction.

Section 2. Section 3 provides a brief theoretical background of the numerical procedure used in the present paper. Flow description and statistics from simulation and experiments are discussed in Section 4. Dynamics of unsteady separation, Reynolds-numbers dependency and characteristic scales are presented in Section 5. Concluding perspectives and remarks are given in Section 6.

2. Flow configuration, methods and experimental conditions

The aim of this section is to provide the flow characteristics and present the experimental techniques used to obtain the sets of data. The x -coordinate is referred as the streamwise direction (pointing downstream), y -coordinate as the cross-stream (upward) and z -coordinate as the spanwise direction. The crest of the bump is taken as the origin of the coordinate system. Instantaneous, ensemble-averaged and fluctuating horizontal and vertical velocity components are denoted by u , v , U , V , u' , and v' , respectively. The Reynolds number considered hereafter is based on the friction velocity u_τ , the half-height H , the kinematic velocity ν , and is noted $Re_\tau = u_\tau \cdot H / \nu$ (obtained at $x^* = -6$).

2.1. Facility and test model

The experimental investigations are conducted in the small hydrodynamic re-circulating water channel of LAMIH (Laboratory of Industrial and Human Automation control, Mechanical engineering and Computer Science). Bottom and sides walls (see Fig. 1) are made in PERSPEX[®] with a minimum number of support braces to maximize optical access. It was originally designed to study wall turbulence phenomena [35]. To control the free-stream velocity, flow is powered by water pumps coupled to a Dc motor drive. The test section has a full height of $2H$ (20 mm) and it operates at a moderate velocity range with a low free stream turbulence intensity (the contraction ratio is up to 1:30). The spanwise dimension of the channel is 150 mm, providing a 7.5 : 1 channel aspect ratio. As sketched in Fig. 1, the flow is tripped at the channel inlet using thin rods (1 mm diameter). For more details about the present experimental apparatus, see Keirsbulck et al. [35]. Boundary layer separation is induced by placing a smooth bump on the bottom wall of the test section at a distance $L = 1250$ mm from the channel inlet. The geometry (shown in Fig. 2) was originally designed by DASSAULT AVIATION to reproduce, for turbulent flows, the pressure gradient of a wing with short attack angle representative of aeronautical industrial applications [7]. The same geometry was considered recently in the numerical investigation of Laval et al. [36] and in the experimental investigation of Passaggia et al. [27]. The bump, used in the present investigation, has a height $h = 6.7$ mm and a characteristic length of $10h$. The bump extends over each channel sidewalls in the spanwise direction.

2.2. Measurement techniques

The unsteady separation process and its associated instability mechanism are known to be sensitive to small perturbations. Therefore, in order to preserve the flow physics, all the experimental techniques employed in the present study are non-intrusive.

Velocity time-series measurements are carried out with a laser Doppler anemometry (LDA) system, mounted on a traverse device. The system consist of the fiberoptic-based optics and its electronics (DANTEC FLOWLITE). Due to a solid wall close to the channel, a back-scatter orientation is used. Signal processing is performed via a DANTEC BSA FLOW software. For all optical techniques, the liquid is seeded with micron-size IRIODIN¹ particles with mean particle diameters on the order of 10–15 μm , with a Stokes number S_{tk} (defined as the ratio of the characteristic time of the particles, τ_p to a characteristic time of the turbulent flow, τ_f) approximatively in the range from 0.001 to 0.01. Furthermore, the relaxation time of the particles it is defined as: $\tau_p = (\rho_p - \rho_f)d_p^2 / (18\mu_f)$ where μ_f is the water dynamic viscosity, ρ_p , ρ_f respectively the particle and the water densities and d_p the mean particle diameter. Concerning the characteristic time of the flow, defined as: $\tau_f = \eta_f / U_c$ where η_f is an estimation of the Kolmogorov scale and U_c the convection velocity estimated to be equal respectively to $0.001H$ and 10% of the free-stream velocity. As a consequence, the flow tracer fidelity in our particle image velocimetry experiments are acceptable since response time of the particles to the motion of the fluid is reasonably short to accurately follow the flow. The velocity profiles are measured at several locations along the test section during 5 min at each point of the profile. Spectral analysis of velocity signals is performed to uncover organized flow structures and determine their characteristics. In this particular case, the associate velocity time-series measurements are carried out with a longer time of 1 h each.

For quantitative flow visualization measurements, both a time-resolved and spatial-resolved Piv systems are used. Two different Piv setups are used in the present study. Both fields of view are illustrated in Fig. 2, the \star symbol will denote hereafter the half height normalization. The cameras are located on the side of the bump. The same particles are used for the Piv and the LDA measurements. The time-resolved setup is used to resolve the dynamic of unsteady vortices induced in the separation area, while the other setup increases the field of view in order to capture the near-wall phenomena with a good spatial resolution. The time-resolved system consists of a QUANTRONIX DARWIN-DUO operating at 528 nm with two-cavities laser and a 12 bit Imager PHANTOM v641 CMOS camera. The camera is able to operate in a single-frame mode with a frame rate of 1450 Hz at full resolution (2560 \times 1600 pixels). The laser beam is collimated and then expanded into an approximately 0.5 mm in thickness sheet.

¹ Pigments sold by Merck Corporation.

The images are recorded at 1450 frames per second in order to have a sufficient temporal resolution to resolve the unsteady vortices dynamic. This set consists of 3000 instantaneous realizations over a period of 2.07 s. The field of view is $12 \times 45 \text{ mm}^2$ covering the entire channel height. The velocity vectors are calculated using an adaptive correlation with 32×32 pixels interrogation windows and a 50% overlap leading to a spatial resolution of $0.02H$. A local median method, included in the Piv software, is employed to eliminate outliers. A 3×3 median filter is also used to smooth the vector fields in order to define the vortical structures in the separated area. An other Piv system was used to obtain a more spatially resolved velocity fields using a larger CCD camera. In this setup, the light sheet is provided by a double-pulsed ND-YAG laser QUANTEL BSLT220 with a 12 bit Imager POWERVIEW 16M camera at the full resolution of 4864×3232 pixels. In those measurements, the data consist of ensembles of 1500 realizations recorded at 1 Hz. The field of view is $20 \times 50 \text{ mm}^2$ covering the full separation area. At the final stage, the interrogation window size was set to 16×16 pixels, corresponding to a spatial resolution of 0.08 mm ($0.008 H$). The relative uncertainties on the mean velocity and on the fluctuation velocity can be estimated respectively to 0.2% and 2% of the free stream velocity.

This study also focuses on the ability of the electrochemical method (see [37] for a thorough review) to analyze the wall-shear stress fluctuation distribution on the bump surface. The experimental method determines the limiting diffusion current at the surface of a platinum microelectrode and it was adapted to study the wall bounded turbulent flow dynamics [35]. The wall-shear stress is experimentally determined using an array of two-segment electrodiffusion microelectrodes ($100 \mu\text{m} \times 500 \mu\text{m}$) placed at different positions above the bump surface (reported in Table 1). The segments are oriented with the longer side perpendicular to the mean flow direction. The two probe segments (introduced by Son and Hanratty [38]) are able to measure the magnitude of wall shear rate, detect the existence of near-wall flow reversal [39,40] and estimate the wall-shear rate signals close the reattachment point [41]. The electrolytic solution used in the present study is a mixture of ferri-ferrocyanide of potassium (10 mol/m^3) and potassium sulphate (240 mol/m^3). The limiting diffusion current is converted to voltage using a KEITHLEY 6514 system electrometer, and acquired using a 12 bit A/D converter from an acquisition system GRAPHTEC GL1000. Wall-shear stress time-series measurements are sampled at 1 kHz using a 500 Hz low-pass anti-aliasing filter during 1 h each. For high-frequency fluctuations of the wall shear rate, the filtering effect of the concentration boundary layer reduces the mass transfer rate fluctuations enabling the use of the linearization theory [42–44]. For an accurate evaluation of the relative wall-shear stress fluctuation, the dynamic behavior can be corrected using the inverse method. This technique is a diffusion-convection equation developed by Mao and Hanratty [45], its methodology for heat transfer problems can be found in literature [46–49]. In our case, the inverse method, based on a sequential estimation ensures a sufficiently good frequency response (above 500 Hz) to resolve dominant frequency peaks and wall-shear stress statistics.

2.3. Flow conditions

In order to define the inflow conditions, experimental velocity measurements were recorded; using LDA, at an unperturbed upstream position of $x^* = -6$ (we recall that x^* is associated with quantities non-dimensionalized by H and the origin is taken at the crest of the bump). Profiles of the streamwise velocity as a function of the wall-normal coordinate are presented in Fig. 3 for a range of Reynolds number from 125 to 730. The profiles obtained, specially at a Reynolds number of $Re_\tau = 605$, agree well with the DNS results from [36], denoted in Fig. 3 with dashed line. The parameters of the upstream velocity profiles are presented in Table 2.

Table 1

Flush-mounted micro-electrodes locations against the Reynolds number based on the friction velocity. L_R denotes the separate length and x^* denotes the probes positions normalized by the half height.

x^*	0.22	0.52	0.62	0.72	0.92	1.03	1.12	1.32	1.42	1.52
Re_τ										
125	0.07	0.17	0.21	0.24	0.31	0.34	0.38	0.44	0.48	0.51
165	0.10	0.23	0.27	0.31	0.40	0.44	0.49	0.57	0.62	0.66
255	0.13	0.30	0.35	0.41	0.53	0.58	0.64	0.75	0.81	0.87
375	0.18	0.43	0.52	0.60	0.77	0.85	0.93	1.10	1.18	1.27

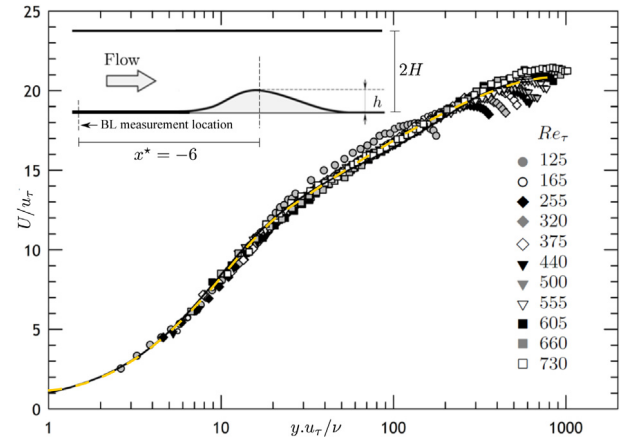


Fig. 3. Profiles of the streamwise velocity against the wall-normal coordinate for various Reynolds-numbers. Dashed line represents DNS results of [36] at $Re_\tau = 617$.

3. Numerical method and theoretical background

3.1. Numerical procedure

Direct numerical simulations (DNS) of converging-diverging channels have been performed, with the exact same geometry, for three Reynolds numbers using the code MFLOPS3D developed by LML. The parameters of the DNS are given in Table 3. The algorithm used for solving the incompressible Navier–Stokes equations is similar to the one described in Marquillie et al. [7]. To take into account the complex geometry of the physical domain, the partial differential operators are transformed using mapping, which has the property of following a profile at the lower wall with a flat surface at the upper wall. Applying this mapping to the momentum and divergence equations, the modified system in the computational coordinates has to be solved in the transformed Cartesian geometry. The three-dimensional Navier–Stokes equations are discretized using respectively eight and fourth orders centered finite differences for the first and second order derivatives in the streamwise x -direction. A pseudo-spectral Chebyshev-collocation method is used in the wall normal y -direction. The spanwise z -direction is assumed periodic and is discretized using a spectral Fourier expansion. The resulting 2D-Poisson equations are solved in parallel using MPI library. Implicit second-order backward Euler differencing is used for time integration, the Cartesian part of the diffusion term is taken implicitly whereas the nonlinear and metric terms (due to the mapping) are evaluated using an explicit second-order Adams–Bashforth scheme. In order to ensure a divergence-free velocity field, a fractional-step method has been adapted to the present formulation of the Navier–Stokes system with coordinate transformation. In order to ensure a divergence-free velocity field a fractional-step method has been adapted to the present formulation of the Navier–Stokes system with coordinate transformation. The

Table 2

Mean-flow parameters. The subscript c and b referred to quantities based on the centerline and on the bulk velocity.

U_c (m s ⁻¹)	U_b (m s ⁻¹)	u_τ (m s ⁻¹)	Re_b ($U_b \times H/\nu$)	Re_τ	$C_b \times 10^3$	Symbols
0.26	0.21	0.0144	3652	125	9.40	●
0.36	0.29	0.0190	5010	165	8.70	○
0.56	0.48	0.0295	8330	255	7.59	◆
0.72	0.62	0.0370	10765	320	7.09	◇
0.88	0.76	0.0430	13265	375	6.38	◇
1.02	0.89	0.0505	15600	440	6.34	▼
1.16	1.01	0.0565	17565	500	6.26	▼
1.32	1.15	0.0640	20090	555	6.14	▽
1.45	1.30	0.0695	22575	605	5.74	■
1.61	1.43	0.0760	24870	660	5.65	■
1.79	1.59	0.0837	27650	730	5.54	□

Table 3

DNS parameters: u_τ is the friction velocity, U_b is the bulk velocity, L_x & L_y & L_z are domain size in streamwise, vertical and spanwise directions, N_x & N_y & N_z are the number of grid points in the corresponding directions and x^* is the streamwise coordinate of the inlet.

Re_τ	u_τ	U_b	L_x	L_y	L_z	N_x	N_y	N_z	x^*
187	0.0576	0.913	4π	2	2π	768	129	384	-5.21
395	0.0501	0.907	4π	2	π	1536	257	384	-3.67
617	0.0494	0.905	4π	2	π	2304	385	576	-5.21

Table 4

Separation points x_s^* , reattachment points x_r^* and separation lengths L_R^* for experimental and DNS results.

Experimental data				DNS data			
Re_τ	L_R^*	x_s^*	x_r^*	Re_τ	L_R^*	x_s^*	x_r^*
165	2.388	0.564	2.952	187	2.917	0.538	3.455
375	1.198	0.510	1.708	395	1.187	0.565	1.752
605	0.764	0.500	1.364	617	0.838	0.547	1.385

metric of the Poisson equation for the pressure correction is taken explicitly and, in practice, few iterations are necessary to recover a pressure correction up to the second order in time which is the overall accuracy of the time marching algorithm. A constant advection condition U_c based on the bulk velocity is used for the outlet and inlet are generated from precursor DNS or highly resolved LES of flat channel flows at Reynolds number equivalent to each DNS of converging-diverging channels. The two boundary conditions only affect the property of the flow in very limited region far from the region of interest.

The inlets are generated from flat channel flows DNS at Reynolds number equivalent to each DNS of converging-diverging channels except for the medium Reynolds number case for which the precursor simulation was a highly resolved LES which does not affect the turbulence statistics in the region of interest subjected to pressure gradient Marquillie et al. [7] and Laval et al. [36].

4. Baseline mean flow description and statistical behavior

It is known, from various experiments [23,24,32], that the separation bubble intermittently changes shape and size with the flapping of the shear layer and strongly depends on the flow regime. In order to establish the characteristics of the separated flow in the channel, we analyze the statistical behavior associated with the velocity fields and the wall shear-stress along the bump at the middle plane of the channel. In this section, numerical and experimental description of flow patterns, such as the separation length or the vorticity thickness, are extracted and compared to the numerical predictions.

4.1. Velocity fields and separation length

The recirculation zone, also referred as the separation bubble, is primarily dominated by a large two-dimensional vortex with a low circulation velocity. In order to visualize the baseline separate flow fields, Fig. 4 shows the normalized mean streamwise velocity U/U_b for both experiments and direct numerical simulations. To have a validation of the numerical data, a comparison between experimental measurements (mean velocity contours from PIV at $Re_\tau = 165, 375$ and 605) and numerical simulations (DNS for Reynolds number $Re_\tau = 187, 395$ and 617) was done. The domain that is considered $-0.3 < x^* < 4.5$ and $0 < y^* < 2$ is the same for both the experiments and simulations. Values of the separation lengths L_R , separation point x_s and reattachment point x_r for both the numerical and experimental data can be found in Table 4. High levels of mean streamwise velocity distributions are nearby the bump crest. Furthermore, for $Re_\tau = 165/187$, the shear layer extends from the bump crest ($x^* = 0$) to $x^* \approx 4$. This value significantly decreases for $Re_\tau = 375/395$ and $Re_\tau = 605/617$, extending downstream the bump crest up to $x^* \approx 2$ and $x^* \approx 1.5$, respectively. The shear layers associated with the latter are significantly thicker than those at $Re_\tau = 165/187$. The location and length of the shear layers for both simulation and experiment are similar, except for $Re_\tau = 165/187$ where a slight difference occurs probably due to spanwise confinement effects [50]. These similarities reveal a good agreement for mean flow properties associated with the recirculation region between experiments and DNS. The separation length (L_R) is plotted in Fig. 5 for all the Reynolds-numbers studied in the present paper, including those from previous numerical investigations (Schiavo et al. [51]).

As already mentioned, it is crucial to predict if a separation exists considering the Reynolds number and the nature of the flow. For that, two cases are observed: no separation (not represented herein) and a separation with reattachment over the bump surface. The recirculation zone behind the bump can be extracted from velocity measurements. The separation length decreases up to an estimated critical value close to $Re_\tau = 1200$. Marquillie et al. [7] observed that, for $Re_\tau = 395$ and $Re_\tau = 617$, the turbulent flow slightly separates on the profile at the lower curved wall and is at the onset of separation at the opposite flat wall (but keeping a positive minimum friction velocity of the order of 0.001 and 0.0015 respectively). The slowing down of the opposite wall is also noticed for the present experiment for all the Reynolds numbers studied (see Fig. 4). This confirms a close agreement between the numerical and experimental results and an accurate prediction of the separation bubble. The presence of a negative level of the mean tangential component of the velocity distribution (U_τ), in the vicinity of the bump surface, highlights the presence of a separation bubble caused by adverse pressure gradients. The development of the normalized mean

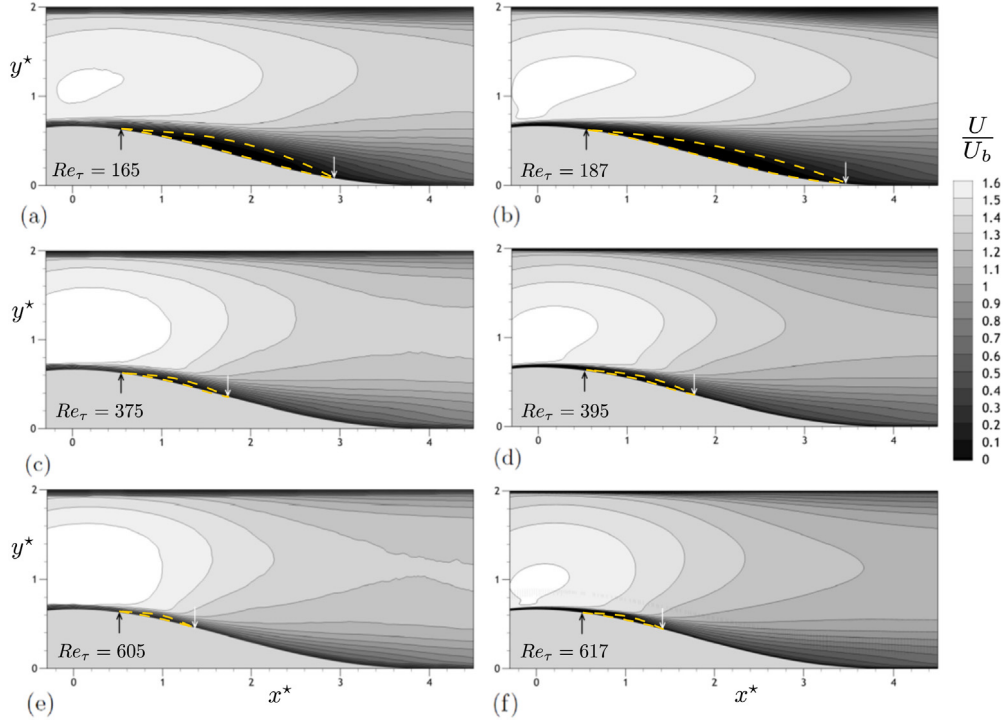


Fig. 4. Contour plots of normalized streamwise velocity (U/U_b): (a) PIV at $Re_\tau = 165$; (b) DNS at $Re_\tau = 187$; (c) PIV at $Re_\tau = 375$; (d) DNS at $Re_\tau = 395$; (e) PIV at $Re_\tau = 605$; (f) DNS at $Re_\tau = 617$. Black arrows denote the separation points and white arrows the reattachment points. Dashed lines denote the separation bubbles for all the cases presented.

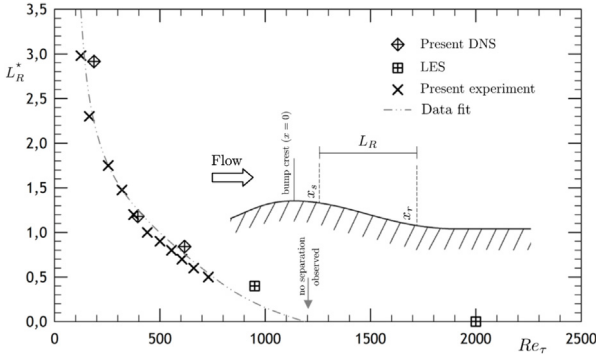


Fig. 5. Normalized separation length, L_R^* , plotted against Re_τ . Cross diamond symbols represent the present DNS data and cross square symbols represent the LES data from [51]. The uncertainty interval of L_R based on the PIV uncertainty is equal to $L_R^* = \pm 0.1$.

tangential component at the channel centerline ($z^* = 0$) for $Re_\tau = 165/187$ can be seen in Fig. 6. The profiles are scaled by the bulk velocity. The direction of the local outward normal of the surface (η) is normalized by the separation length. Two main features can be observed in the mean velocity profiles: the development of the recirculation area over the bump surface and the shear-layer generated by the bump crest on the profiles near the wall (see Fig. 4). Once more, similar patterns are observed for both experiment and simulation. The negative level close to the wall depicts a large recirculation area for $Re_\tau = 165/187$. This area decreases for higher Reynolds-numbers (see Fig. 4). Fig. 4 (a) and (b) show a similar normalized flow profiles in the separation area, even though the separation length is not exactly at the same position along the bump.

The free shear layer plays an important role in the dynamics of the separated bubble, since the interaction of large eddy

structures with the wall in the reattachment region are formed upstream this area. Therefore, it is worth analyzing the streamwise evolution of the shear layer characteristics. The growth of the separated shear layer may be described by the vorticity thickness, δ_ω , as defined by Brown and Roshko [17] and given by:

$$\delta_\omega(x) = \max_\eta \left(\frac{\Delta U_\zeta}{\partial U_\zeta / \partial \eta} \right), \quad (1)$$

where ΔU_ζ is the difference between the maximum wall-tangential velocity on the high speed side of the shear layer, $U_{\zeta max}$, and the minimum wall-tangential velocity on the low speed side, $U_{\zeta min}$. η denotes the direction of the local outward normal of the wall. Upstream the reattachment point ($(x - x_s)/L_R < 1$), $U_{\zeta min}$ reaches negative values in the reverse-flow region and $U_{\zeta max}$ increases over the bulk velocity, U_b , up to 50% (see Fig. 6). Two regions are evidenced in the streamwise evolution of the vorticity thickness, seen in Fig. 6, for the experimental data ($Re_\tau = 165$) and numerical simulations ($Re_\tau = 187, 375$ and 617). Note that the experimental extraction of the vorticity thickness, for Reynolds numbers higher than $Re_\tau = 165$, is not possible with a satisfying accuracy due to the narrow thickness of the shear layer. The first region is located between $(x - x_s)/L_R = 0$ and 0.4 where the growth of the mixing layer is exponential as predicted by linear stability theory in the case of planar mixing layers. The second one ($(x - x_s)/L_R > 0.4$), evidenced in Fig. 6 and obtained from our experimental data, is wider and characterized by a nearly linear rate $d\delta_\omega/dx = 0.17 - 0.275$. The value obtained with the lowest Reynolds number is higher than those observed in classical planar mixing layer where the growth rate was equal to 0.17 ([52]). For $(x - x_s)/L_R \approx 1$, the shear layer is affected by the reattachment process and the vorticity thickness reaches a maximum value before it strongly decreases. This result is in accordance with the observations of Cherry et al. [14] (see Fig. 8).

In order to validate the DNS results, a comparison, shown in Fig. 7, between experiment and numerical statistics is done and

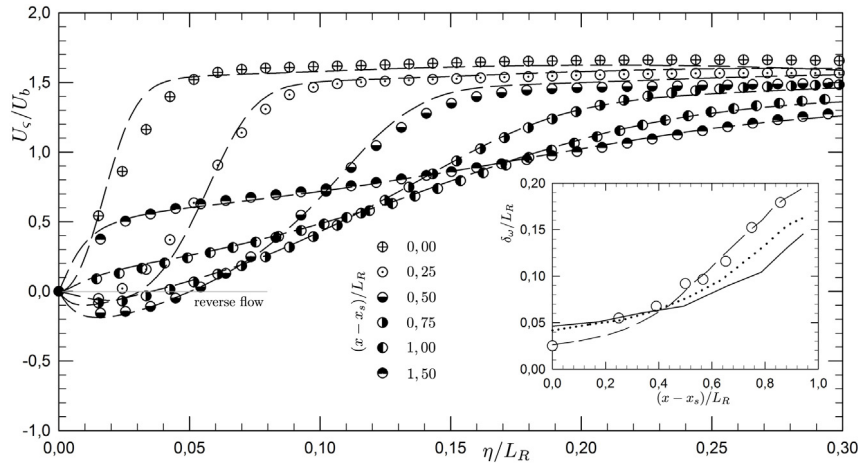


Fig. 6. Normalized mean tangential component U_ξ at the channel symmetry plane ($z^* = 0$) against η/L_R . The direction of the local outward normal of the surface for $Re_\tau = 165/187$. The inset plot is the normalized vorticity thickness against $(x - x_s)/L_R$, x_s denotes the separation abscissa. \circ represent experimental data for $Re_\tau = 165$. Lines represent numerical data (solid line; $Re_\tau = 617$, short-dashed lines; $Re_\tau = 395$ and medium-dashed lines; $Re_\tau = 187$).

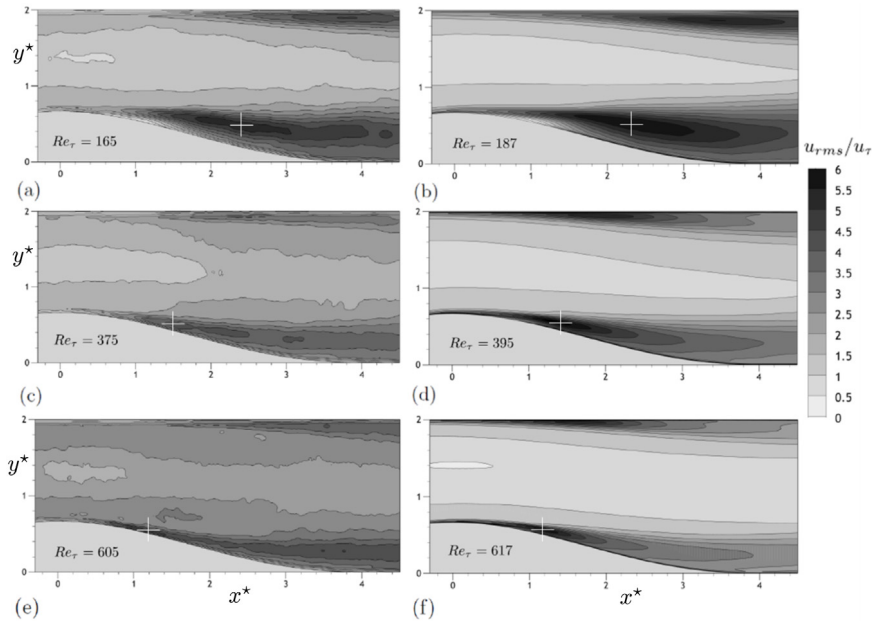


Fig. 7. Contour plots of normalized streamwise r.m.s. velocity (u_{rms}/u_τ): (a) PIV at $Re_\tau = 165$; (b) DNS at $Re_\tau = 187$; (c) PIV at $Re_\tau = 375$; (d) DNS at $Re_\tau = 395$; (e) PIV at $Re_\tau = 605$; (f) DNS at $Re_\tau = 617$.

focus on the normalized streamwise r.m.s. velocity fluctuations for three equivalent Reynolds numbers i.e. $Re_\tau = 165/187$, $375/395$ and $605/617$. A global agreement can be observed between the experiments and the numerical results. The location of the highest r.m.s values for the three Reynolds number is denoted in Fig. 7 by a white cross symbol. For $Re_\tau = 165/187$, the peak locations and magnitudes for the simulation and the experiment agree well. However, at $Re_\tau = 375/395$ and $Re_\tau = 605/617$, the peaks are correctly located, but the magnitudes at the vicinity of the bump surface are lower for the experiments than for the simulations. This is due to the limited resolution of PIV with respect to the smallest coherent structures. A detailed analysis of the vortices in 2D planes of the DNS at the largest Reynolds number ($Re_\tau = 617$) has been performed. Both experiments and DNS exhibit the same general behavior for fluctuations. At $Re_\tau = 605/617$, the separation area is significantly shorter and thicker than at $Re_\tau = 165/187$ while the overall form of the distribution

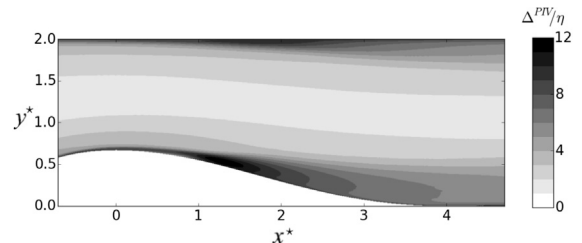


Fig. 8. Distribution of the ratio Δ^{PIV}/η for $Re_\tau = 605/617$.

at $Re_\tau = 165/187$ is similar to that at the higher Reynolds-number. The loci of the r.m.s. maxima has moved upstream from $x^* = 2.5$ up to $x^* = 1.3$ for $Re_\tau = 605/617$.

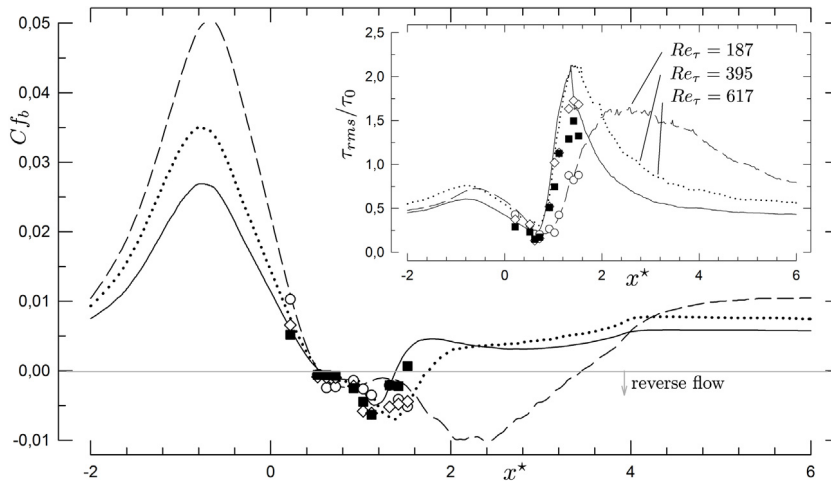


Fig. 9. Skin friction coefficient over the bump surface plotted against x^* for three Reynolds-numbers (numerical and experimental dataset). Relative intensity of the wall shear-stress fluctuations are also plotted against x^* . τ_0 denotes the mean wall shear stress evaluate at $x^* = -6$. \circ $Re_\tau = 165$, \blacklozenge $Re_\tau = 375$ and ∇ $Re_\tau = 605$. Lines represent numerical data (solid line; $Re_\tau = 617$, short-dashed lines; $Re_\tau = 395$ and medium-dashed lines; $Re_\tau = 187$).

4.2. Behavior of the wall-shear stress statistics

The mean skin friction coefficient over the bump surface is plotted against x^* in Fig. 9 for $Re_\tau = 165, 375$ and 605 . This figure includes also DNS results at $Re_\tau = 187, 395$ and 617 for comparison purposes. Statistical values are deduced from the wall-shear stress time histories using the electrochemical technique at the streamwise locations defined in Table 1. The mean skin friction obtained from experimental data agrees with the simulation. Measurements confirm the high value of the skin friction coefficient before the crest region. The separation region is also underlined by secondary peaks values observed from the DNS data just after the bump crest at $x^* = 2.3, 1.4$ and 1.2 , for $Re_\tau = 165/187, 375/395$ and $605/617$ respectively. These peaks correspond to the maximum values of the streamwise r.m.s. velocity denoted by cross symbols in Fig. 7. Moreover, the present results show a strong Reynolds number dependence and a trend toward a constant value, indicating that the flow reaches equilibrium conditions.

In order to quantify the near wall unsteadiness, the r.m.s. wall-shear stress above the bump is analyzed. The relative intensity of the wall-shear stress fluctuations over the bump surface, given in the inset of Fig. 9, is reported against x^* for experimental and numerical data. Despite a slight shift of the friction coefficient in the separation region, the latter figure shows that the experimental results agree well with the numerical simulations. This minor difference is due to the limiting experimental frequency responses of the electrochemical technique, that are not able to reproduce correctly the high unsteadiness levels occurring at the reverse flow region. Low fluctuations of the wall-shear stress are observed before the separation. These fluctuations increase at the separation region and remains high until $x^* \simeq 6$ for the lower Reynolds numbers. Strong secondary peaks of the mean bulk skin friction coefficient, previously mentioned, coincide with the minimal values of the relative intensity of the wall-shear stress fluctuations.

5. Study of the dynamics of separated turbulent flow

5.1. Shedding and non-linear interactions of shear layer eddies

In order to enhance the dominant scales, for each region of the flow, and to investigate the characteristic frequencies embedded in the unsteady separated flow fields, we perform spectral analysis at various locations along the bump for different Reynolds

numbers. Power spectra densities (P.S.D) of the vertical fluctuating velocity component are sensitive to instability phenomena associated with spanwise structures. Therefore, we use P.S.D of the vertical velocity component in order to investigate the development of shear layer instabilities. P.S.D are computed using the Welch method with a Hamming window, an overlap of 75% and an acquisition time of 1 h each. Normalized P.S.D for various representative locations are presented in a logarithmic scale in Fig. 10a for the streamwise stations inside the separation area. For $Re_\tau = 165$, the frequency distribution exhibits a broadband hump phenomenon, denoted by a + symbol in figure Fig. 10a. In particular, the humps are shifted toward lower frequencies when probes locations are moved from $x/L_R = 0.43$ to $x/L_R = 1.52$. For $1.5 < x < 1.8$, the humps are centered around a fixed frequency. When rescaled by the bump height and for Reynolds numbers ranging from 125 to 255, the fundamental frequency is $S_f \approx 0.2$ (where the centerline velocity U_c is considered) of the same order than the vortex shedding phenomenon reported in the literature for various flow configurations (Sigurdson [18]). For $Re_\tau > 320$, Fig. 10b shows that the humps are broader and less defined than those obtained for lower Reynolds numbers. These observations indicate that the shape and motion of vortices becomes more irregular for higher Reynolds numbers (*i.e.* the vortex-shedding acts in broadband frequency).

A sequence of characteristic snapshots of the spanwise component of the fluctuating vorticity ω_z from time-resolved PIV measurements is shown Fig. 11 for $Re_\tau = 125$. The local fluctuating vorticity is used herein to identify vortices in the flow field and to show that the main dominant large structures are deformed, sheared, broken, and periodically transported along the shear layer. This figure illustrates the development and the spatial organization of the vortex-shedding from the shear layer. The negative fluctuating spanwise vorticity corresponds to clockwise rotation of the vortices, as the positive fluctuations correspond to the counter-clockwise rotation. For this Reynolds number, $Re_\tau = 125$, the propagating vortices are nearly circular with a radius of approximately $H/2$ stretching into elliptical shapes further downstream. This phenomenon is also previously observed by Mollicone et al. [10].

The fluctuating spanwise vorticity field, shown in Fig. 11(a-e), consists of alternate regions of positive and negative values. A vortex structure convection without self-interaction but with a strong collective interaction [52] can be observed. A region of high vorticity inside the shear layer shows that the structures remain dissociated during a cycle. White circles represent the cores

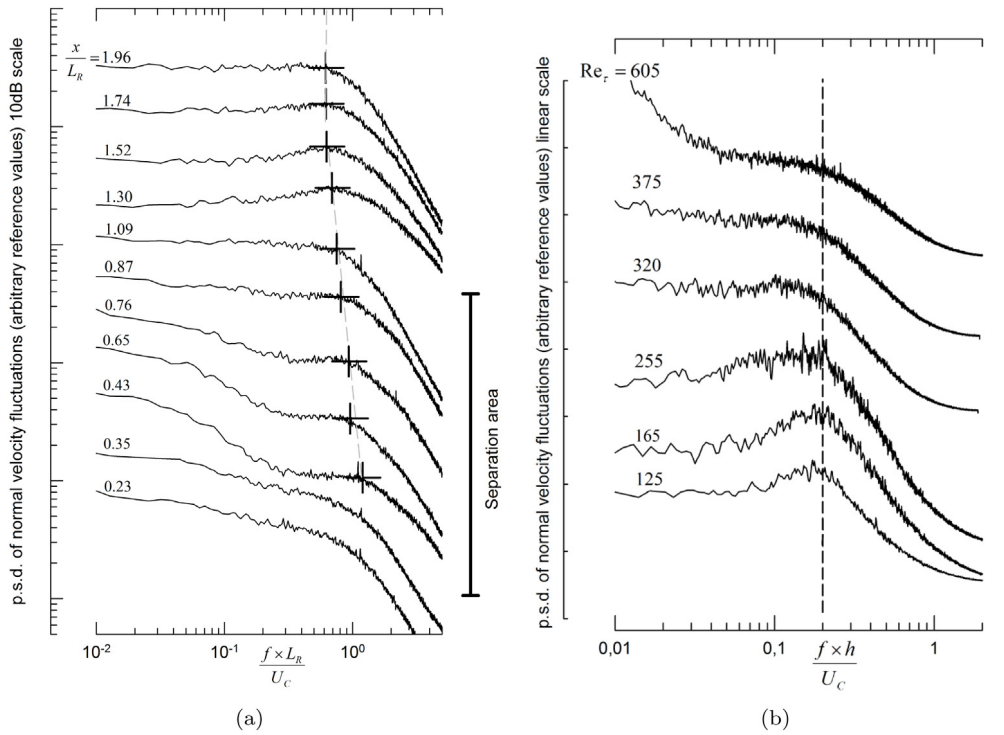


Fig. 10. Power spectral densities (P.S.D) of the vertical fluctuating velocity component, v' , (a) at various x/L_R location along to the shear layer and at an elevation corresponding to the maximum of the velocity gradient locations for $Re_\tau = 165$ (b) at $x/L_R \approx 1.5$ for various Reynolds numbers. h/U_c is used in order to normalize the frequency and P.S.D are plotted with arbitrary reference scale. Measurements are obtained from the laser Doppler anemometry. The + symbol denotes the evolution of spectral emergences against the dimensionless probe positions. Measurements are obtained from the laser Doppler anemometry.

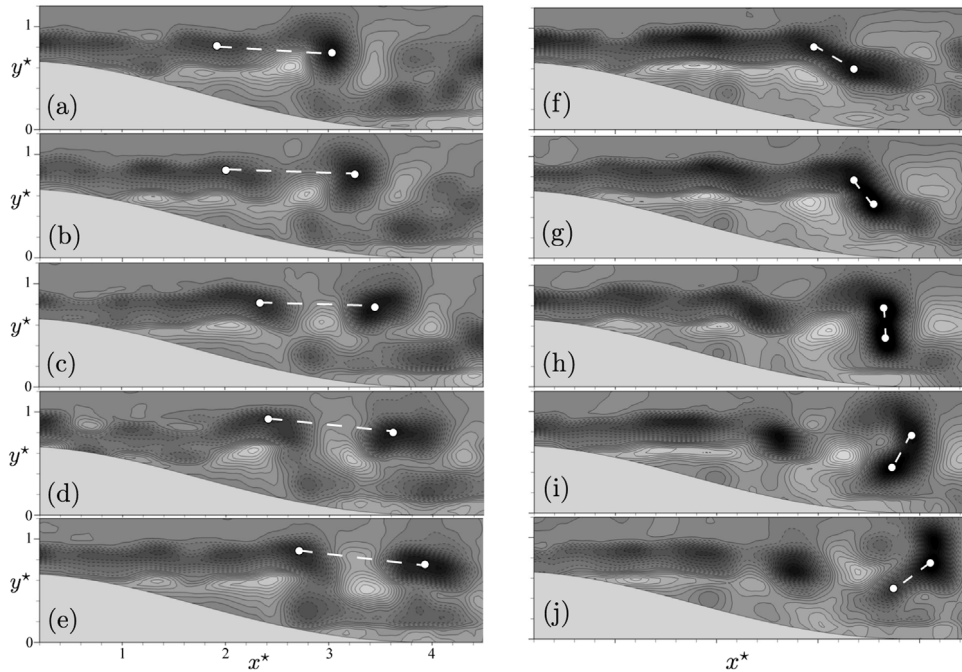


Fig. 11. Two samples of the fluctuating vorticity field from the TR-Piv at $Re_\tau = 125$ showing different phases of the same shear layer vortex without (a to e) and with (f to j) self-interacting. Time steps follow from top to bottom and the normalized time interval between snapshot is $\Delta t.U_b/h = 0.0216$. Arbitrary scale. \circ denotes dominant vorticity centers. The two vortices cores pointed out have a clockwise rotation.

of the propagating vortices for different consecutive time instants. The vortex core is defined as the position of the maximum magnitude of the spanwise vorticity. These cores are initially located closer to the centerline of the shear layer. The lines connecting the vortex cores correspond to a typical path followed by the shed

vortices. The relatively uniform spacing between vortex cores is attributed to an almost constant vortex shedding frequency, which also confirms that the vortex-shedding moves with a constant convection velocity. The general features of unsteady events depicted in Fig. 11 are repetitive. However, some features, such as

the period, the vortex size and shape and the self-interaction, vary substantially from one structure to the next. An example of coherent structures interaction is illustrated in Fig. 11(f–j). Based on the mechanism observed previously, it is expected that the identified vortices (with clockwise rotation) convect without further interaction. But, in this case, the vortex-shedding, which is driven by the low frequency oscillation, subsequently diverges away. This behavior is due to the reverse flow moving toward the wall leading, in this particular case, to a merging of the coherent structures with the vortex development just downstream the shear layer. This phenomenon occurs more often when the Reynolds number increases and can explain the broadband behavior of the shedding for higher Reynolds numbers.

5.2. Low-frequency flapping

The influence of the mean recirculation region onto the low-frequency dynamics was identified in a very recent study carried out by [53], for the shock/wave turbulent boundary layer interaction. In particular, the authors investigated the linear global stability of the mean flow obtained by LES. They found low frequency modes that are strongly localized in the recirculation area and exhibit close correspondence with the breathing of the bubble observed in the LES. In this context, the influence of the recirculation zone onto the low frequency motions is of major interest in the study of turbulent separated flows. Hereafter, we investigate low-frequency dynamics (flapping motion) in the light of weighted power spectrum density of the wall-shear stress and characteristic scales of the mean separated flow. In Fig. 12, weighted power spectral density distribution are shown for several distances x/L_R and Reynolds-number ($Re_\tau = 125, 165, 255$ and 375). The hump, obtained by the power spectra of the normal fluctuating velocities in the shear-layer, correspond to the frequency of shear-layer vortices. However, other humps can be found at values lower than those obtained from the shear-layer vortices frequency. These humps, underlined by plus symbols in Fig. 12, are clearly observed until $x/L_R \approx 0.6$. For higher distances, $x/L_R > 1$, the peaks seem to merge and disappear. As mentioned previously, when the distance from the bump crest increase, the frequency range, associated to the shear-layer vortices, moves toward lower values. This deviation can be seen by the dashed-lines in Fig. 12. In contrast to the high-frequency shear-layer vortices, the low frequency humps are centered at a constant frequency $S_t = 0.12$ (denoted by vertical dashed-lines in Fig. 12). This characteristic frequency is consistent with those obtained in previous experimental studies ([14] and [12]) and corresponds to the flapping of the shear-layer. The low flapping frequencies and shear-layer vortices appear to be confined near the bump crest region.

In figure 12, we observe that the humps associated with both flapping motion and vortex shedding phenomenon emerge for probes localized in the recirculation region for $125 < Re_\tau < 375$. The humps flatten as the probes are moved away from the region associated with mean separation. This characteristic curve is in agreement with the measurements observed in a separated bubble for a backward-facing step configuration [54]. These broadband humps are less visible compared to a laminar flow regime, where it is easier to detect the phenomena (see Passaglia et al. [27]).

The broadband humps, which is characteristic of the flow spectra in the shear layers, vanishes downstream the shear layer. In the light of the present findings, the presence of flapping in this flow regime has not been detected before. Indeed, in the present study, the flapping could not be detected in the velocity spectra but it is revealed only in the wall shear stress spectra.

To give some insight about the driving mechanism and its link with mean flow properties, we use the model derived by Piponniau et al. [21]. The latter model suggests an universal parameter $S_t/g(r) \approx [5 - 6]$ with:

$$g(r) = \frac{\delta'_w}{2} \frac{2(1-r)}{1+r} \left((1-r)C + \frac{r}{2} \right)$$

where δ'_w is the spreading rate of the mixing layer and r is the reverse flow intensity. These values are associated with the two-dimensional mean flow. In particular, Piponniau et al. [21] argue that $g(r)$ is a universal function relying on classical similarity properties of plane mixing layer. As underlined by Piponniau et al. [21], C is fixed to 0.14. In the latter expression, we neglect compressibility effects. When using mean quantities associated with DNS database for $Re_\tau = 165, 395$ and 617 we obtain for $S_t/g(r)$ values that are comprised between 4.75 and 5.4 for $S_t = 0.12$. Hence, it may suggest that the two-dimensional mechanism proposed by Piponniau et al. [21] that relies on an instantaneous imbalance between the entrainment rate from the bubble and the reinjection of fluid near the reattachment line is also the driving process of the flapping phenomenon for a separated flow behind a bump.

5.3. Modal decomposition: DMD analysis

In the previous section, the analysis of experimental data, to calculate the weighted power spectrum density of the wall-shear stress fluctuations, has shown two main points. First, the spectrum is broadband, reflecting highly turbulent activity. Second, the two frequency ranges are statistically favored: the first one at low frequency, $S_t \sim 0.1$, corresponding to a flapping dynamics and the second one, $S_t \sim 2$, mainly linked to the dynamics of the shear-layer generated by the separated boundary-layer downstream of the bump. The study of the dynamics of these two particular frequency ranges and in particular the link between the frequency and the spatial location of the associated mode can allow us to better understand the different physical mechanisms involved. Several modal decompositions can be used for this investigation, the most well known being the Proper Orthogonal Decomposition (POD). The POD allows to order modes by level of decreasing energy. However this is not our objective here because a frequency decomposition is more natural when we want to compare with experiments. Recently Rowley et al. [55] and Schmid [56] proposed a Dynamics Modal Decomposition (DMD) which has the advantage to be a frequency modal decomposition easily accessible (see Appendix for a deeply study of this technique). The advantage of the DMD, relative to other frequency decomposition such as for example Fourier decomposition, is to better grasp the real physical mechanisms, in particular for transient or non-equilibrium phenomena. The DMD can be used with both experimental and numerical data. The main constraint is to have access to sufficiently time-resolved data. In the present case, experimental data is well resolved temporally over a long time, but poorly resolved in space, when the DNS data is well resolved both in space and time but limited to a short integration time. The objective is to characterize the spatial nature of the disturbance for a given frequency, this is why the DMD analysis is performed on DNS data. This implies that only the medium frequencies are available, flapping phenomenon is then unresolved. The DMD analysis was conducted only for the case with a Reynolds number $Re_\tau = 617$.

The computational domain for DMD analysis is linked to the bump in local coordinates system $(x_b/L_R, y_b/L_R, z_b/L_R)$ and shown in Fig. 13 by a red rectangular box. The lengths of the domain are: $(L_{x_b}, L_{y_b}, L_{z_b})/L_R = (3.31, 0.5, \pi/2)$. The computational grid is a regular mesh of $N_{x_b} \times N_{y_b} \times N_{z_b} = 250 \times 75 \times 235$ points.

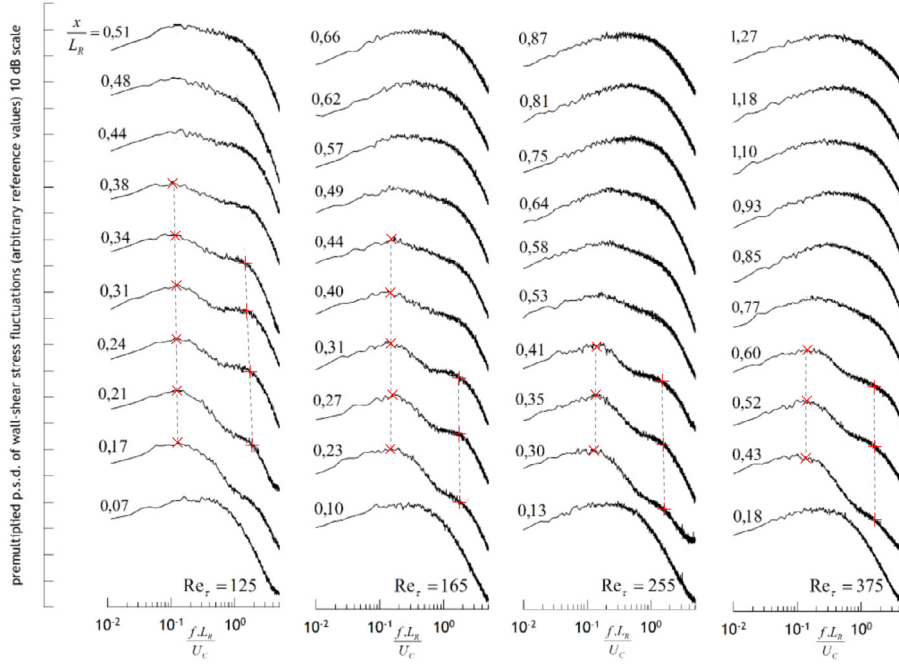


Fig. 12. Weighted power spectrum density of the wall-shear stress fluctuations at various Reynolds-number against the distance x/L_R . + and \times symbols denotes the spectrum peaks. The vertical dashed line shows the normalized low-frequency 0,12 and the inclined dashed lines denotes the evolution of the secondary spectrum peaks. Measurements are obtained from the electrochemical method.

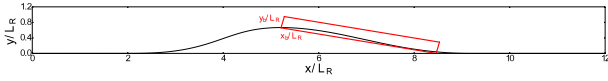


Fig. 13. Computational domain for DMD analysis. $(x/L_R; y/L_R)$ are the global coordinates. $(x_b/L_R; y_b/L_R)$ are the local coordinates linked to the bump.

The DMD modes are processed as follows: (i) the numerical data initially given in global coordinates system $(x/L_R, y/L_R, z/L_R)$ are interpolated in DMD grid $(x_b/L_R, y_b/L_R, z_b/L_R)$. (ii) The velocity component (u, v, w) are decomposed into $\mathbf{u} = \mathbf{u}_{\parallel} + \mathbf{u}_{\perp}$ where \mathbf{u}_{\parallel} and \mathbf{u}_{\perp} are the parallel and perpendicular velocity components to the direction of the mean flow $\bar{\mathbf{U}}$ respectively. These two components are given by:

$$\mathbf{u}_{\parallel} = \frac{(\mathbf{u} \cdot \bar{\mathbf{U}})}{\|\bar{\mathbf{U}}\|^2} \bar{\mathbf{U}} \quad \text{and} \quad \mathbf{u}_{\perp} = \mathbf{u} - \mathbf{u}_{\parallel}.$$

(iii) The DMD analysis was performed in the referential (x_b, y_b, z_b) then projected in the referential (x, y, z) . Details of the method are summarized in [Appendix](#). The DMD analysis is based on a sequence of $N_s = 930$ snapshots of the velocity field sampled at a constant sampling period $\Delta t_s = 0.06$. Preliminary tests have shown that these parameters $(\Delta t_s, N_s)$ are able to converge fairly well the frequency range $[0.1; 10]$.

Fig. 14-(Left) depicts the eigenspectrum of the approximate Koopman eigenvalues λ_j . Almost all eigenvalues lie on the unit circle, indicating that the dynamics is statistically stationary and well converged. **Fig. 14-(Right)** shows the kinetic energy of each mode with respect to the associated Strouhal number S_t (in a logarithmic scale). The turbulent nature of the flow generates a continuous field of peaks ranging from high to low frequencies. This result is in good agreement with the PSD analysis previously discussed. In the previous sections, the analysis of temporal signals from the DNS has shown that there is a range of frequencies around $S_t \sim 2$ where the dynamic implies coherent structures related to the shear-layer. As this frequency range is well resolved by the DMD analysis, it is thus possible to extract the DMD mode

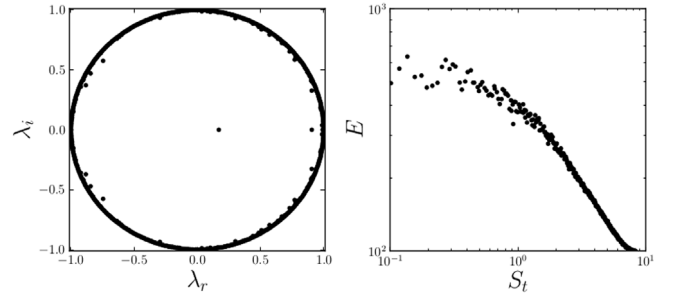


Fig. 14. (Left): Spectrum of the Dynamic Mode Decomposition. (Right): The normalized kinetic energy norm versus the Strouhal number. $Re_{\tau} = 617$.



Fig. 15. The DMD mode for $S_t = 2$ computed from the flow around the bump, illustrated using two opposite contours of the perpendicular velocity component \mathbf{u}_{\perp} .

for this particular frequency. **Fig. 15** depicts the spatial distribution of the DMD mode for $S_t = 2$ and for the wall normal velocity component. The velocity field of the DMD mode is clearly related to a Kelvin-Helmholtz mode with a parallel wavelength of about $1/4L_R$. It is found that despite a fully turbulent flow upstream

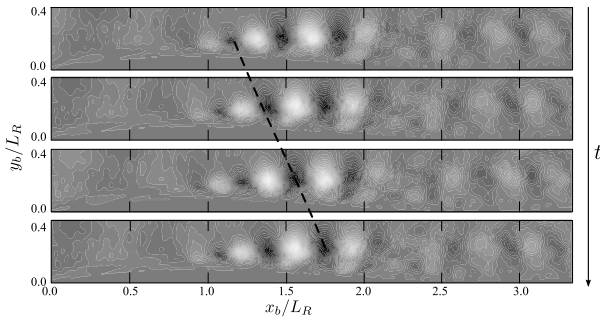


Fig. 16. Evolution of the perpendicular component of velocity of the (K-H) mode for a Strouhal number $S_t = 2$ over one period T .

of the bump, the K-H mode is almost two-dimensional in the first part of the separated zone. In this area, the mode is spatially amplified. Further downstream, the K-H mode quickly loses its two-dimensional nature and complex three-dimensional structures are observed that quickly lose their coherence. As shown in the next section (Fig. 17), this zone is characterized by a vortex-shedding phenomenon where the frequency no longer evolves with the streamwise direction. The frequency of vortex-shedding is determined by the value of the frequency of the K-H mode when the vortex-shedding starts. This abscissa where the K-H modes are released depends on the frequency. The higher is the frequency, the earlier the vortex-shedding phenomenon starts. In order to clearly identify the nature of the modes in the first part of the separated zone, the computation of the convection velocity of these modes has been achieved. Fig. 16 shows the evolution of the Kelvin-Helmholtz mode at $S_t = 2$ over one period T . To improve the coherence of the mode, the velocity field has been previously averaged in z direction. The advection velocity of the structures is closed to $U_c/2$, which corresponds perfectly to the convection velocity of shear-layer instabilities observed in the literature.

One may also remark some similarities between the modes obtained by the DMD analysis carried out in the present study for a turbulent flow and the global modes computed by Ehrenstein and Gallaire [24] in a laminar regime for the same flow case. It suggests the persistence of such instabilities in the turbulent regime.

6. Conclusion and final remarks

The present analysis combining numerical and experimental approaches aimed to deeply understand how the Reynolds-number affects the mean separation length and how the turbulent regime may change flow unsteadiness characteristics. The results indicated that, for turbulent flows, the frequency range is the typical combination of flapping phenomenon and shear-layer instabilities. High-resolution Piv and electrochemical measurements have been conducted in a Reynolds-number range of 125–730. These results were compared to direct numerical simulations, at similar Reynolds numbers ($Re_\tau = 187, 395, 617$). Flow baseline statistics from both simulations and experiments were compared in order to validate the DNS prediction. The velocity fields along the bump were analyzed and showed the existence of a separated region, clearly observed for moderate Reynolds numbers. A deep analysis of self-sustained oscillations and convective instabilities of the shear-layer was also addressed. Two high frequency shear layer instabilities, shedding phenomena and K-H oscillations, and one low-frequency, flapping motion, are identified. Both PSD of vertical velocity component and wall shear stress were used to investigate unsteadiness of the separate shear layer. It showed that characteristic frequencies detected for low

Reynolds numbers and classically observed in the literature, still exist for high Reynolds numbers. A peak at the fundamental frequency corroborated the existence of shedding of the shear layer vortices. Weighted power spectrum density of the wall-shear stress fluctuations were computed to investigate the near wall unsteadiness. Flapping frequencies could only be detected in the wall shear stress spectra, and appeared to be confined near the crest bump region. Results showed a broadband spectrum and two frequency ranges statistically being favored. This broad band peak can be explained by the non-periodic self-interacting vortex pairing phenomena; observed from the Tr-Piv measurements.

Considering the substantial variation of flow characteristics within the investigated range of Reynolds numbers, a length scale, linked to the separation length flapping phenomenon, as opposed to a geometric model dimension, would be more appropriate. Frequency peaks, extracted from Figs. 10 & 12 for all the Reynolds-numbers, as a function of x/L_R are plotted in Fig. 17. For this case, the flapping exhibits a nearly constant normalized low-frequency of $S_t = 0.12$. Variations of Reynolds-number influence the instability. For values of S_t around 2, the shear-layer vortex frequencies decrease due to the shear-layer instabilities and are strongly dependent of the Reynolds-number. Investigation on both experimental and numerical data did not yield to provide suitable scaling for the shear-layer instabilities, because the very restricted region where the phenomena occurs, for high Reynolds numbers, is difficult to analyze. However, in our case, the frequency of this phenomena can be scaled by the vorticity thickness. This scaling led to a same dimensionless frequency value $f\delta_\omega/U_c \approx 0.1 \pm 0.02$ for the three lower Reynolds numbers, but the latter is lower compared to those classically obtained in the literature. We propose the bump height, H , as an alternative length scale for the shedding scaling. The variation of the resulting universal normalized frequency fH/U_c is shown in the upset of Fig. 17. This scaling dramatically reduces the variation of the scaled vortex shedding frequency. A summary of the experimental results obtained in the present study is reported in Fig. 17. In fact, despite a minor scatter, the data collapse into a universal normalized frequency of about $fH/U_c \approx 0.2$, which is in good agreement with that reported in the literature.

From these analyses, it appears that unsteadiness observed for the same configuration in the laminar regime by Passaglia et al. [27] are also detected in the turbulent regime. Nevertheless, some discrepancies exist. For instance, the flapping phenomenon is of the order $S_t = 0.12$ in the turbulent regime. When considering the laminar case studied by Passaglia et al. [27] we obtained $S_t \approx 0.5$ which is significantly higher. It suggests that a different mechanism as the one proposed by Gallaire et al. [32] occurs in the turbulent regime. In addition, the good agreement between dimensionless frequency derived from the model given by Pionniau et al. [21] and results provided by the same authors gave some confidence that a two-dimensional mechanism based on fluid entrainment along the mixing layer is also active for this configuration. The latter mechanism generates low-frequency motions associated with successive contractions and expansions of the recirculation zone.

It should be also consistent with the recent numerical study carried out by Mollicone et al. [10] based on the DNS database of Mollicone et al. [9] for a similar configuration. The previous authors through the Generalized Kolmogorov equation GKE give further support onto a strong correlation between vortical structure developing onto the shear layer and the recirculation region. As underlined by Mollicone et al. [10], these coherent motions are trapped by the recirculation region while being advected in the bubble. They may eventually disappear and reform again at the top of the recirculation area.

DMD analysis was conducted for one numerical data set ($Re_\tau = 617$) to characterize the spatial nature of the disturbances. Results

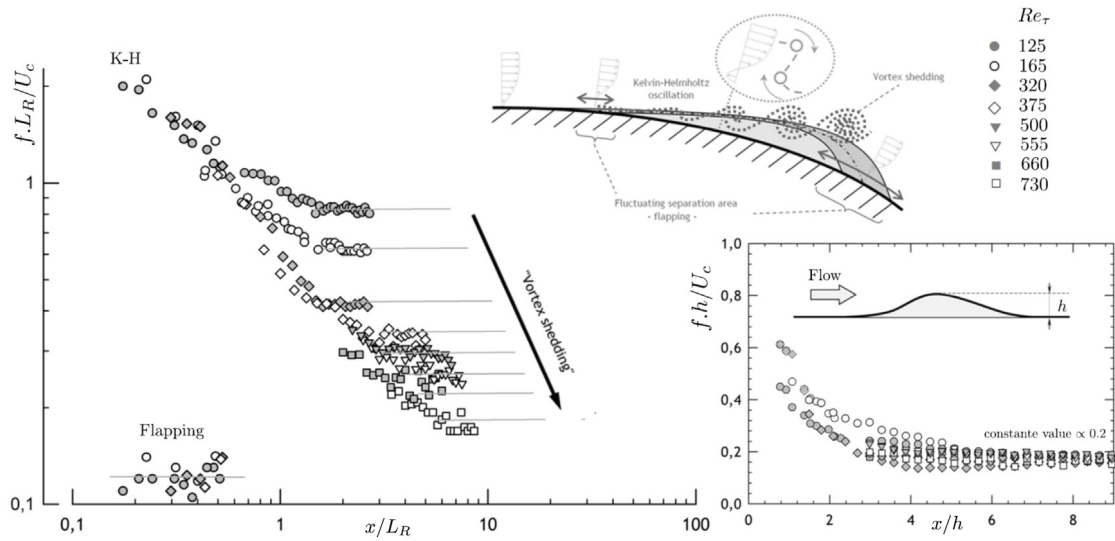


Fig. 17. Normalized frequencies peaks plotted against the distance from the separation location above the bump surface. The significant peaks are extracted from the wall-shear stress and from the velocity spectra. H denotes here the bump height.

from DMD analysis clearly highlighted the coherent shear-layer instability phenomenon, similarly as the one observed in the laminar regime by Gallaire et al. [32] that it provides strong evidence of the persistence of such instabilities in the turbulent regime. Furthermore, the convection speed observed from DNS database is consistent with experimental observations.

Until now, the present study is the first one to deeply explore unsteadiness presented in a turbulent flow regime and demonstrates the persistence of such phenomena even for high Reynolds numbers. This paper opens the way for an harmonic forcing flow control based on the modulation of the studied coherent motions.

Acknowledgments

This work was carried out within the framework of the CNRS Research Federation on Ground Transports and Mobility, in articulation with the Elsat2020 project supported by the European Community, the French Ministry of Higher Education and Research, the Hauts de France Regional Council. This work was granted access to the HPC resources of IDRIS under the allocation 021741 made by GENCI (Grand Equipement National de Calcul Intensif). The authors gratefully acknowledge the support of these institutions.

Appendix. Dynamic modal decomposition (Dmd)

The modal decomposition of fluid dynamics is a frequently employed technique, capable of providing tools for studying dominant and coherent structures in turbulent flows. The coherent structures represent spatially or temporally evolving vortical motions, either growing with one rate, oscillating with one frequency or containing the largest possible kinetic energy. A complex turbulent flow often consists of a superposition of such coherent structures, whose development is responsible for the bulk mass, energy transfer or hydrodynamic instability. DMD is a data-driven computational technique capable of extracting dynamical information from flow fields measured in physical experiments or generated by direct numerical simulations. DMD is a powerful method of spectral decomposition, built to represent statistically recurring and transients events. The DMD modes are extracted from the data snapshots and a unique frequency is associated to each mode.

The coherent features of turbulent separated bubble (TSB) behind the bump are identified by modal decomposition tech-

niques in order to describe the underlying mechanism of TSB. An advantage of modal decomposition is the possibility to reduce the large scale dynamics to a fewer number of degrees of freedom. To extract the coherent motion from a given dataset, we consider a sequence of m discretized and equi-distributed velocity fields $\mathbf{u}_j = \mathbf{u}(\mathbf{x}_i, t_j) \in \mathbb{R}^n$, $t_j = j\Delta t$, $j = 0, 1, \dots, m-1$ as

$$\mathbf{U}_m = [\mathbf{u}_0, \mathbf{u}_1, \dots, \mathbf{u}_{m-1}] \in \mathbb{R}^{n \times m}, \quad (\text{A.1})$$

where n is the total number of degrees of freedom at one time instant (number of grid points multiplied by the number of velocity components). This number is usually large compared to the number of snapshots m in the flow problem, $n \gg m$. In modal decomposition, the flow dynamics is splitted into space and time dependent parts as

$$\mathbf{u}(\mathbf{x}_i, t_j) = \sum_{k=0}^{m-1} \phi_k(\mathbf{x}_i) \mathbf{a}_k(t_j), \quad (\text{A.2})$$

where $\phi_k(\mathbf{x}_i)$, $k = 0, \dots, m-1$ is spatial basis (the modes) and $\mathbf{a}_k = \mathbf{a}_k(t_j)$ are temporal coefficients (amplitudes). This decomposition is not unique and depends on the choice of the base ϕ_k . In dynamic mode decomposition (DMD), the snapshots are generated by a dynamical system. It is possible, without explicit knowledge of the evolution operator, to extract frequencies, growth rates, and their related spatial structures. DMD splits the flow into different spatial modes at a given frequency. Rowley et al. [55] present the theoretical framework to compute the Koopman decomposition from a finite sequence of snapshots. Schmid [56] provides a more stable method to compute dynamic modes: the DMD algorithm. To compute this decomposition, a sufficiently long, but finite time series of snapshots is considered. A time-evolving physical situation may be approximated by the action of a linear operator to the flow field \mathbf{u}_j such that

$$\mathbf{u}(\mathbf{x}_i, t_{j+1}) = \mathbf{u}_{j+1} = e^{\tilde{\mathbf{A}}\Delta t} \mathbf{u}_j = \mathbf{A} \mathbf{u}_j, \quad (\text{A.3})$$

where $\mathbf{A} = e^{\tilde{\mathbf{A}}\Delta t}$ is the evolution operator. It is then possible to write

$$\mathbf{u}(\mathbf{x}_i, t_j) = \sum_{k=0}^{m-1} \phi_k(\mathbf{x}_i) \mathbf{a}_k(t_j) = \sum_{k=0}^{m-1} \phi_k(\mathbf{x}_i) e^{i\omega_k j \Delta t} = \sum_{k=0}^{m-1} \phi_k(\mathbf{x}_i) \lambda_k^j, \quad (\text{A.4})$$

where $i\omega_k$ and λ_k are the eigenvalues of the matrices $\tilde{\mathbf{A}}$ and \mathbf{A} , respectively, and the ϕ_k are the corresponding eigenvectors. The relation linking the eigenvalues λ_k and the more familiar complex frequencies $i\omega_k$ is

$$\lambda_k = e^{i\omega_k \Delta t}$$

It is then possible to write $\phi_k = \mathbf{v}_k d_k$ where $\mathbf{v}_k^T \mathbf{M} \mathbf{v}_k = 1$. We define d_k as the amplitude and d_k^2 as the energy of the dynamic mode ϕ_k .

References

- [1] P. Joseph, X. Amandolese, C. Edouard, J.L. Aider, Flow control using mems pulsed micro-jets on the ahmed body, *Exp. Fluids* 54 (1) (2013) 1–12.
- [2] S.L. Yang, G.R. Spedding, Separation control by external acoustic excitation at low Reynolds numbers, *AIAA J.* 51 (6) (1991) 1506–1515.
- [3] J. Dandois, E. Garnier, P. Sagaut, Numerical simulation of active separation control by a synthetic jet, *J. Fluid Mech.* 574 (2007) 25–58.
- [4] M. Gad-el Hak, D. Bushnell, Separation control: review, *J. Fluids Eng.* 130 (1991) 5–30.
- [5] S. Song, D.B. Degraaff, J.K. Eaton, Experimental study of a separating, reattaching, and redeveloping flow over a smoothly contoured ramp, *Int. J. Heat Fluid Flow* 21 (2000) 512–519.
- [6] D.R. Webster, D.B. DeGraaffe, J.K. Eaton, Turbulence characteristics of a boundary layer over a two-dimensional bump, *J. Fluid Mech.* 320 (1996) 53.
- [7] M. Marquillie, J.P. Laval, R. Dolganov, Direct numerical simulation of separated channel flows with a smooth profile, *J. Turbulence.* 9 (2008) 1–23.
- [8] J.B.R. Loureiro, F.T. Pinho, A.P. Silva Freire, Near wall characterization of the flow over a two-dimensional steep smooth hill, *Exp. Fluids* 42 (2007) 441–457.
- [9] J.-P. Mollicone, F. Battista, P. Gualtieri, M. Casciola, Effect of geometry and Reynolds number on the turbulent separated flow behind a bulge in a channel, *J. Fluid Mech.* 823 (2017) 100–133.
- [10] J.-P. Mollicone, F. Battista, P. Gualtieri, M. Casciola, Turbulence dynamics in separated flows: the generalised Kolmogorov equation for inhomogeneous anisotropic conditions, *J. Fluid Mech.* 841 (2018) 1012–1039.
- [11] H. Le, P. Moin, J. Kim, Direct numerical simulation of turbulent flow over a backward-facing step, *J. Fluid Mech.* 330 (1997) 349–374.
- [12] M. Kiya, M. Sasaki, Structure of large-scale vortices and unsteady reverse flow in the reattaching zone of a turbulent separation bubble, *J. Fluid Mech.* 154 (1985) 463–491.
- [13] E. Lamballais, J. Silvestrini, S. Laizet, Direct numerical simulation of flow separation behind a rounded leading edge: Study of curvature effects, *Int. J. Heat Fluid Flow* 31 (3) (2010) 241–253.
- [14] N.J. Cherry, R. Hiller, M.P. Latour, Unsteady measurements in a separating and reattaching flow, *J. Fluid Mech.* 46 (1984) 144–157.
- [15] J.K. Eaton, J.P. Johnston, A review of research on subsonic turbulent flow reattachment, *AIAA J.* 19 (1981) 1093–1100.
- [16] D.K. Tafti, S.P. Vanka, A three-dimensional numerical study of flow separation and reattachment on a blunt plate, *Phys. Fluids* 2 (1991) 2887.
- [17] G.L. Brown, A. Roshko, On density effects and large structure in turbulent mixing layers, *J. Fluid Mech.* 64 (4) (1974) 775–816.
- [18] L.W. Sigurdson, The structure and control of a turbulent reattaching flow, *J. Fluid Mech.* 298 (1995) 139–165.
- [19] M. Marquillie, U. Ehrenstein, J.-p. Laval, Instability of streaks in wall turbulence with adverse pressure gradient, *J. Fluid Mech.* 681 (2011) 205–240.
- [20] C. Cossu, G. Pujals, S. Depardon, Optimal transient growth and very large scale structures in turbulent boundary layers, *J. Fluid Mech.* 619 (2009) 79–94.
- [21] S. Pionnoniau, J.P. Dussauge, J.F. Debiève, P. Dupont, A simple model of low-frequency unsteadiness in shock-induced separation, *J. Fluid Mech.* 629 (2009) 87–108.
- [22] A.V. Dovgal, V.V. Kozlov, A. Michalke, Laminar boundary layer separation: instability and associated phenomena, *Prog. Aerosp. Sci.* 30 (1) (1994) 61–94.
- [23] M. Marquillie, U. Ehrenstein, On the onset of nonlinear oscillations in a separating boundary-layer flow, *J. Fluid Mech.* 490 (2003) 169–188.
- [24] U. Ehrenstein, F. Gallaire, Two-dimensional global low-frequency oscillations in a separating boundary-layer flow, *J. Fluid Mech.* 614 (2008) 315–327.
- [25] P. Huerre, P.A. Monkewitz, Local and global instabilities in spatially developing flows, *Annu. Rev. Fluid Mech.* 22 (1) (1990) 473–537.
- [26] J.-M. Chomaz, Global stabilities in spatially developing flows: non-normality and nonlinearity, *Ann. Rev. Fluid Mech.* 37 (2005) 357–392.
- [27] P. Passaggia, T. Leweke, U. Ehrenstein, Transverse instability and low-frequency flapping in incompressible separated boundary layer flows: an experimental study, *J. Fluid Mech.* 730 (2012) 363–373.
- [28] O. Marxen, U. Rist, Mean flow deformation in a laminar separation bubble: separation and stability characteristics, *J. Fluid Mech.* 660 (2010) 37–54.
- [29] F. Alizard, S. Cherubini, J.-Ch. Robinet, Sensitivity and optimal forcing response in separated boundary layer flows, *Phys. Fluids.* 21 (2009) 064108.
- [30] O. Marquet, D. Sipp, J.-M. Chomaz, L. Jacquin, Amplifier and resonator dynamics of a low-Reynolds-number recirculation bubble in a global framework, *J. Fluid Mech.* 605 (2008) 429–443.
- [31] H.M. Blackburn, D. Barkley, S.J. Sherwin, Convective instability and transient growth in flow over a backward facing step, *J. Fluid Mech.* 603 (2008) 271–304.
- [32] F. Gallaire, M. Marquillie, U. Ehrenstein, Three-dimensional transverse instabilities in detached boundary layers, *J. Fluid Mech.* 571 (2007) 221–233.
- [33] D. Barkley, M. Gabriela, M. Gomes, R.D. Henderson, Three-dimensional instability in flow over a backward-facing step, *J. Fluid Mech.* 473 (2002) 167–190.
- [34] J.-Ch. Robinet, Instabilities in laminar separation bubbles, *Focus Fluids J. Fluid Mech.* 732 (2013) 1–4.
- [35] L. Keirsbulck, L. Labraga, M. Gad-el Hak, Statistical properties of wall-shear-stress fluctuations in turbulent channel flows, *Int. J. Heat and Fluid Flow* 37 (2012) 1–8.
- [36] J.P. Laval, M. Marquillie, U. Ehrenstein, On the relation between kinetic energy production in adverse-pressure gradient wall turbulence and streak instability, *J. Turbul.* 13 (21) (2012) 1–19.
- [37] T. Hanratty, J. Campbell, Measurement of wall shear stress, in: R.J. Goldstein (Ed.), *Fluid Mechanics Measurements*, Hemisphere Publishing Co, 1983, pp. 559–615.
- [38] J.S. Son, T.J. Hanratty, Velocity gradients at the wall for flow around a cylinder at Reynolds numbers from 5×10^3 to 10^5 , *J. Fluid Mech.* 35 (1969) 353–368.
- [39] J. Tihon, V. Tovchigrechko, V. Sobolik, O. Wein, Electrodiffusion detection of the near-wall flow reversal in liquid films at the regime of solitary waves, *J. Appl. Electrochem.* 33 (2003) 577–587.
- [40] J. Tihon, V. Penkavova, J. Havlica, M. Simcik, The transitional backward-facing step flow in a water channel with variable expansion geometry, *Exp. Therm. Fluid Sci.* 40 (2012) 112–125.
- [41] J. Tihon, V. Penkavova, J. Vejrazka, Wall shear stress induced by a large bubble rising in an inclined rectangular channel, *Int. J. Multiph. Flow.* 67 (2014) 76–87.
- [42] A. Ambari, C. Deslouis, B. Tribollet, Frequency response of mass transfer rate in a modulated flow at electrochemical probes, *Int. J. Heat Mass Transfer* 29 (1985) 35–45.
- [43] J. Tihon, J. Legrand, P. Legentilhomme, Dynamics of electrodiffusion probes in developing annular flows, *Exp. Fluids* 20 (2) (1995) 131–134.
- [44] S. Sobolik, O. Wein, J. Cermak, Simultaneous measurement of film thickness and wall shear stress in wavy flow of non-Newtonian liquids, *Collect. Czech. Chem. Commun.* 52 (1987) 913.
- [45] Z. Mao, T. Hanratty, Analysis of wall shear stress probes in large amplitude unsteady flows, *Int. J. Heat Mass Transfer* 34 (1991) 281–290.
- [46] S. Chantasiriwan, Comparison of three sequential function specification algorithms for the inverse heat conduction problem, *Int. Commun. Heat Mass Transfer* 26 (1999) 115–124.
- [47] D.A. Tortorelli, P. Michaleris, Design sensitivity analysis: Overview and review, *Inverse Probl. Eng.* (1994) 71–105.
- [48] S. Chantasiriwan, An algorithm for solving multidimensional inverse heat conduction, *Int. J. Heat Mass Transfer* 44 (20) (1991) 3823–3832.
- [49] J.V. Beck, B. Blackwell, C.R. St-Clair, *Inverse Heat Conduction*, Wiley, New York, 1985.
- [50] V.D. Brederode, P. Bradshaw, Three-Dimensional Flow in Nominally Two-Dimensional Separation Bubbles Part 1: Flow Behind a Rearward-Facing Step, *Tech. Rep. Imperial College Aero Report 72-19*, Department of Aero. Imperial College, London/UK, 1972.
- [51] L.A. Schiavo, A.B. Jesus, W.R. Wolf, J.L. Azevedo, A study of turbulent flows in 2d channels using large eddy simulations, in: 22nd International Congress of Mechanical Engineering, November 3-7, Ribeiro Preto, SP, Brazil, 2013, 2013.
- [52] C.-M. Ho, L.-S. Huang, Subharmonics and vortex merging in mixing layers, *J. Fluid Mech.* 119 (1982) 443–473.
- [53] J.W. Nichols, J. Larsson, M. Bernardini, S. Pirozzoli, Stability and modal analysis of shock/boundary layer interactions, *Theor. Comput. Fluid Dyn.* 31 (2017) 33–50.

- [54] H. Le, Sung, Characteristics of wall pressure fluctuation in separated flows over a backward-facing step. Part I: Time-mean statistics and cross-spectral analyses, *Exp. Fluids* 30 (2001) 262–272.
- [55] C.W. Rowley, V. Mezić, S. Bagheri, P. Schlatter, D.S. Henningson, Spectral analysis of nonlinear flows, *J. Fluid Mech.* 641 (2003) 115–127.
- [56] P.J. Schmid, Dynamic mode decomposition of numerical and experimental data, *J. Fluid Mech.* 656 (2010) 5–28.